

Quantum-preserving telecom conversion of atomic biphotons

Ling-Chun Chen, Chang-Wei Lin, Jiun-Shiuan Shiu, Wei-Lin Chen, Yi-Che Wang, and Yong-Fan Chen*

¹*Department of Physics, National Cheng Kung University, Tainan 70101, Taiwan*

²*Center for Quantum Frontiers of Research & Technology, Tainan 70101, Taiwan*

(Dated: March 10, 2026)

We experimentally demonstrate telecom frequency conversion of atomic biphotons using a diamond-type atomic ensemble. By spectrally engineering heralded photons and optimizing the atomic converter, efficient conversion is achieved while preserving the temporal waveform and non-classical antibunching behavior. The converted photons retain strong quantum correlations and well-defined wavepackets, demonstrating preservation of dynamical quantum properties beyond photon-statistics-based benchmarks. The measured performance agrees with a microscopic model that captures the spectral acceptance and parameter dependence of the converter. These results establish a practical interface between atomic photon sources and telecom fiber networks, enabling quantum interference and distributed quantum communication.

Introduction. Photons serve as ideal flying qubits for quantum communication, distributed computing, and long-distance networking [1–6]. Among various physical platforms, atomic ensembles based on spontaneous four-wave mixing (SFWM) provide a versatile route to generating narrowband biphotons with long coherence times [7–12]. Such ultranarrow bandwidth and extended coherence length are essential for efficient quantum storage and synchronization of remote atomic nodes [13–15]. However, most atomic transitions lie in the visible or near-infrared regime, creating a spectral mismatch with low-loss telecom fiber channels.

Two source-level approaches have been pursued to bridge this gap. Telecom-band photons can be directly generated through atomic cascade transitions and related schemes [16–20], offering narrow linewidth and intrinsic compatibility with atomic systems. However, the spectral and temporal properties of cascade emission are largely determined by atomic structure and are therefore difficult to engineer. Alternatively, narrowband telecom photon sources have been realized using nonlinear crystals with cavity enhancement [21, 22]. While these platforms provide broader tunability, achieving high spectral purity typically requires high-finesse cavities, which reduces brightness and increases system complexity. Consequently, achieving flexible spectral control while maintaining high efficiency and strong compatibility with atomic quantum interfaces remains challenging.

A different approach is telecom frequency conversion, which translates photon wavelength and, under proper spectral matching, can preserve the temporal waveform and quantum correlations of narrowband photons. In resonant atomic media, this process provides narrow linewidths and suppression of broadband noise, enabling high signal-to-noise operation without complex filtering [23–26]. Diamond-type atomic frequency conversion has been implemented in DLCZ-type quantum memory architectures and demonstrates strong background suppression and compatibility with atomic systems [27, 28].

Conversion efficiencies approaching 80% have recently been achieved using weak coherent inputs [29], and theoretical studies indicate that this configuration can operate as a quantum frequency converter in the steady-state regime [30]. Nevertheless, most demonstrations emphasize steady-state efficiency and photon-statistics benchmarks, while direct verification of temporal-waveform preservation in the single-photon regime remains limited. This issue is particularly important for SFWM biphotons, where time-resolved wavepackets and strong temporal correlations are essential for quantum interference and networking protocols.

Preserving the temporal waveform and ensuring spectral compatibility are crucial for high-visibility Hong–Ou–Mandel interference and efficient Bell-state measurements, which underpin entanglement swapping and quantum repeater architectures [31–34]. In addition, mismatch between the photon bandwidth and the acceptance bandwidth of the conversion system can degrade both conversion efficiency and mode fidelity. A systematic experimental investigation of this spectral constraint in resonant atomic systems is still lacking.

In this Letter, we demonstrate telecom frequency conversion of atomic-resonance biphotons in the single-photon regime using a diamond-type atomic ensemble. By tailoring the spectral bandwidth of heralded photons to match the finite acceptance window of the converter, we achieve high conversion efficiency while preserving the temporal waveform and nonclassical antibunching behavior. The converted photons maintain strong time-resolved correlations and well-defined wavepackets. These results provide a time-resolved validation of quantum preservation beyond photon-statistics-based characterization and establish practical guidelines for high-fidelity conversion of narrowband quantum light in hybrid quantum networks.

Experimental setup. To prepare the quantum light source, heralded single photons are generated via double- Λ SFWM in a cold ^{87}Rb ensemble, as shown in Fig. 1(a). The process is driven by two pump fields, a far-detuned 795 nm laser with Rabi frequency Ω_1 and detuning Δ_1 , and a resonant 780 nm laser with Rabi frequency Ω_2 .

* yfchen@mail.ncku.edu.tw

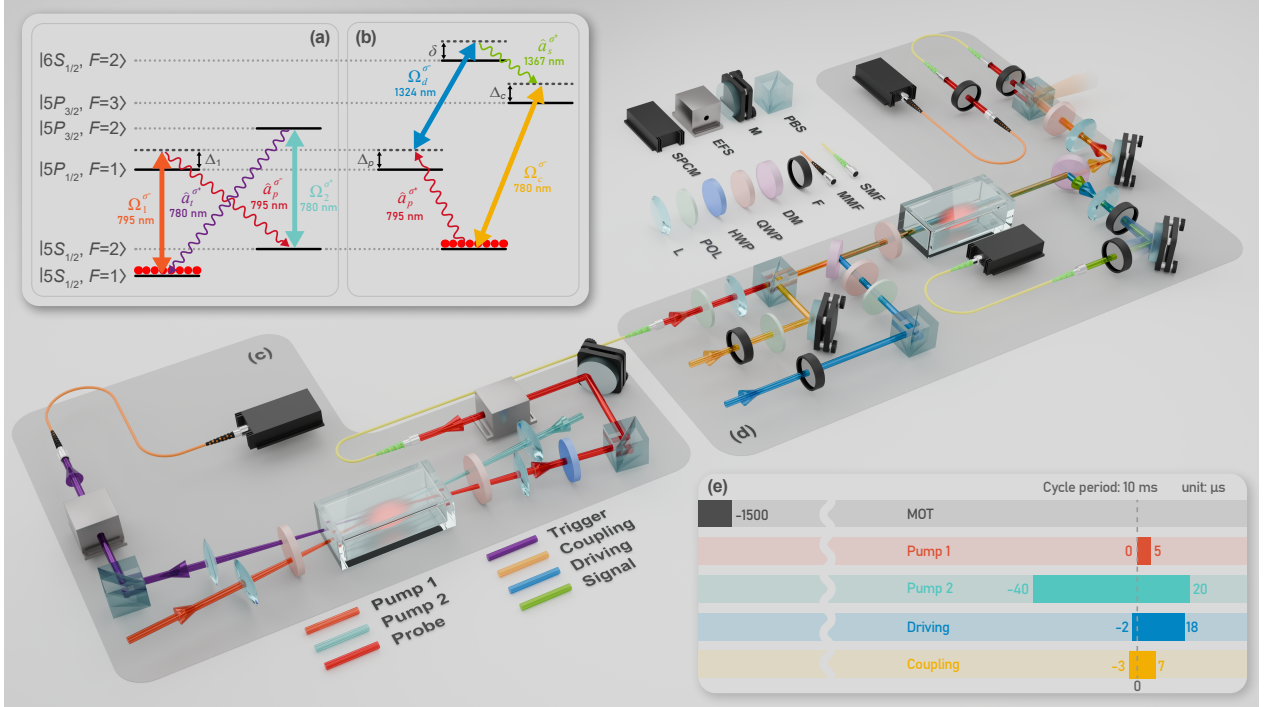


FIG. 1. Experimental architecture of the atomic biphoton source and the telecom frequency conversion platform. (a) and (b) show the energy-level configurations of the double- Λ SFWM source and the diamond-type conversion process. The fields Ω_1 , Ω_2 , \hat{a}_p , \hat{a}_t , Ω_c , Ω_d , and \hat{a}_s denote pump 1, pump 2, probe, trigger, coupling, driving, and the converted signal field. (c) and (d) illustrate the corresponding experimental implementations. F, filter; DM, dichroic mirror; EFS, etalon filter set; HWP, half-wave plate; L, lens; M, mirror; PBS, polarizing beam splitter; POL, polarizer; QWP, quarter-wave plate; SPCM, single-photon counting module; SMF, single-mode fiber; MMF, multi-mode fiber. (e) Timing sequence illustrating the synchronization between heralded photon preparation and the conversion process.

These pumps address the σ^- and σ^+ transitions and generate a σ^- -polarized probe photon \hat{a}_p together with a σ^+ -polarized trigger photon \hat{a}_t .

The probe photon \hat{a}_p serves as the input to the diamond-type telecom frequency conversion, as illustrated in Fig. 1(b). In contrast to the multi-Zeeman structure used in the generation stage, the conversion stage operates on a single isolated Zeeman transition, and the atoms are optically pumped into the $|5S_{1/2}, F=2, m_F=-2\rangle$ ground state [29]. This configuration stabilizes the population distribution and suppresses unwanted optical pumping, thereby improving the robustness and reproducibility of the conversion process. A σ^- -polarized driving field Ω_d at 1324 nm together with a σ^- -polarized coupling field Ω_c at 780 nm is applied to realize this single-transition diamond-type configuration. The probe field \hat{a}_p inherits the detuning $\Delta_p = \Delta_1$ from the SFWM process and is prepared with σ^+ polarization. Under this polarization configuration, spin-angular-momentum conservation yields a σ^+ -polarized telecom signal field \hat{a}_s at 1367 nm. The conversion efficiency is optimized by tuning the one-photon detunings Δ_d and Δ_c together with the two-photon detuning $\delta = \Delta_p + \Delta_d$.

The biphoton source and the conversion system are implemented in two spatially separated cold-atom ensembles, as shown in Figs. 1(c) and 1(d). In the generation

stage, the trigger and probe photons are emitted with strong temporal correlations within the biphoton coherence time. Either photon can in principle be converted. However, converting the trigger photon requires tuning Ω_2 in the SFWM process. This modification changes the nonlinear coupling strength and the spectral response. As a result, waveform distortion appears and the pairing ratio is reduced [35]. In contrast, the probe frequency can be tuned by adjusting Ω_1 . Such tuning mainly shifts the spectral response while preserving stable SFWM operation and strong correlations. This property enables flexible spectral engineering while maintaining stable SFWM operation and strong correlations. The probe photon is therefore chosen as the conversion input here.

To realize strictly heralded operation, a 20 m optical fiber delay corresponding to about 100 ns is introduced in the probe path. Within the biphoton temporal waveform the trigger photon is emitted after the probe photon. The delay therefore allows the trigger photon to be detected before the probe photon enters the converter. The detection event projects the probe field onto a heralded single-photon state with clear antibunching [1]. This condition is essential for reliable quantum conversion.

The optical layouts follow our previous demonstrations [10, 29]. Strong filtering is applied to suppress leakage from the control fields. In the visible path, a polarization

beam splitter and bandpass filters provide 136 dB isolation. The net collection efficiency is 24% before detection by a Si-based single-photon counting module (SPCM). In the telecom path, spectral and spatial filtering suppress the driving field by 135 dB. The converted photons are collected into a single-mode fiber with an efficiency of 57% and detected by an InGaAs-based SPCM. Temporal correlations between trigger and signal photons are recorded using a time-of-flight multiscaler.

Figure 1(e) shows the timing sequence of the experiment. The system operates at a repetition rate of 100 Hz with a 10 ms cycle. During the measurement window the cooling laser fields and magnetic field are switched off to eliminate perturbations from the trapping configuration. After optical pumping with the Ω_2 pump field, biphoton generation is initiated by a 5 μ s pulse of the Ω_1 pump field. In the conversion stage the coupling and driving fields are applied to cover the probe arrival. The coupling field is turned on 3 μ s earlier to enhance optical pumping into the target ground state.

Theoretical model. To characterize the quantum correlations and benchmark the conversion performance, we employ a microscopic open-quantum-system model for the coupled atomic and optical fields. Detailed treatments of the SFWM and frequency conversion processes are given in Refs. [10, 30]. Solving the coupled equations yields the trigger and probe field operators \hat{a}_t and \hat{a}_p . The photon generation rate is defined as $R_l = (c/L)\langle\hat{a}_l^\dagger\hat{a}_l\rangle$, where $l = t, p$. The normalized cross-correlation function between the trigger and probe photons is

$$g_{t-p}^{(2)}(\tau) = \frac{\langle\hat{a}_t^\dagger(t)\hat{a}_p^\dagger(t+\tau)\hat{a}_p(t+\tau)\hat{a}_t(t)\rangle}{\langle\hat{a}_t^\dagger(t)\hat{a}_t(t)\rangle\langle\hat{a}_p^\dagger(t+\tau)\hat{a}_p(t+\tau)\rangle} = 1 + \frac{(L/c)^2}{R_t R_p} \left| \langle\hat{a}_t^\dagger(t)\hat{a}_p^\dagger(t+\tau)\rangle \right|^2. \quad (1)$$

The unity term in Eq. (1) originates from accidental coincidences between independent photons. The second term represents the biphoton temporal wavepacket and corresponds to the two-photon probability amplitude of the correlated emission process. A dominant contribution from this term indicates strong quantum correlations and clear deviation from classical statistics.

The cross-correlation function $g_{t-p}^{(2)}(\tau)$ is directly linked to the purity of heralded single photons. A key metric is the zero-delay conditional autocorrelation function $g_{p-p|t}^{(2)}(\tau)$ [1], which can be written as

$$g_{p-p|t}^{(2)}(\tau) = \frac{4g_{t-p}^{(2)}(\tau) - 2}{\left[g_{t-p}^{(2)}(\tau)\right]^2}. \quad (2)$$

Increasing the cross correlation suppresses $g_{p-p|t}^{(2)}$ toward zero, which demonstrates sub-Poissonian photon statistics. As the delay τ increases, $g_{t-p}^{(2)}$ approaches unity because the temporal correlation is lost. In this limit $g_{p-p|t}^{(2)}$

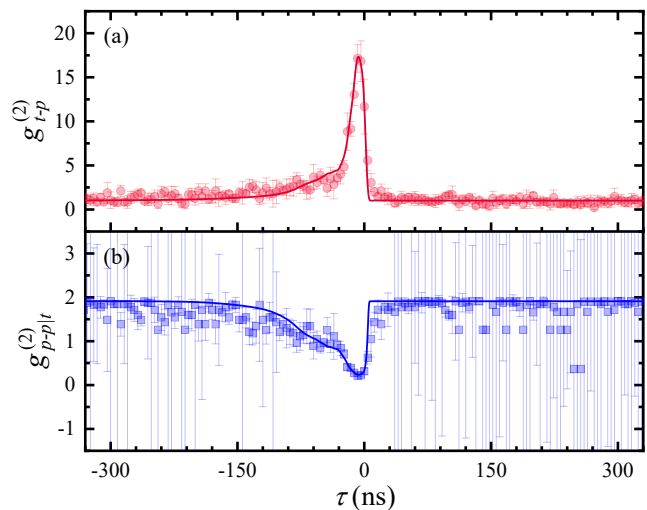


FIG. 2. Benchmarking of the heralded single-photon source. (a) Normalized cross-correlation $g_{t-p}^{(2)}(\tau)$ between the trigger and probe photons, demonstrating strong temporal quantum correlations. (b) Conditional autocorrelation $g_{p-p|t}^{(2)}(\tau)$ of the heralded probe photon, confirming sub-Poissonian statistics and high single-photon purity. Circles and squares represent experimental data and solid curves show theoretical predictions. The parameters are OD = 8, $\Omega_1 = 0.9\Gamma$, $\Omega_2 = 4\Gamma$, and $\Delta_1 = -4\Gamma$. Error bars indicate one standard deviation.

approaches 2, reflecting the thermal statistics of uncorrelated fields.

To account for realistic experimental imperfections including dark counts and optical leakage, we introduce the channel purity P_l for each detection channel. This quantity is defined as the ratio between genuine SFWM signal counts and the total detected counts. The measured cross-correlation function is then modified as

$$g_{t-p}^{(2)}(\tau) \rightarrow P_t P_p \left[g_{t-p}^{(2)}(\tau) - 1 \right] + 1. \quad (3)$$

The conditional autocorrelation must be corrected accordingly. Expressed in terms of the ideal cross correlation, the measured value becomes

$$g_{p-p|t}^{(2)}(\tau) \rightarrow \frac{1 + P_p^2 + 2P_t P_p (1 + P_p) \left[g_{t-p}^{(2)}(\tau) - 1 \right]}{\left\{ P_t P_p \left[g_{t-p}^{(2)}(\tau) - 1 \right] + 1 \right\}^2}. \quad (4)$$

Detailed derivations of these expressions are given in the Supplemental Material.

Heralded probe photons. Figure 2(a) shows the normalized cross-correlation function between the trigger and probe photons, $g_{t-p}^{(2)}(\tau)$. The biphoton source operates at an optical depth (OD) of 8. The pump Rabi frequencies are $\Omega_1 = 0.9\Gamma$ and $\Omega_2 = 4\Gamma$, with a detuning $\Delta_1 = -4\Gamma$. The ground-state decoherence rate is $\gamma_{21} = 0.001\Gamma$, where $\Gamma = 2\pi \times 6$ MHz. The theoretical prediction agrees well with the experimental data. Error bars represent the standard deviation from four independent measurements of 15 min each. After correcting

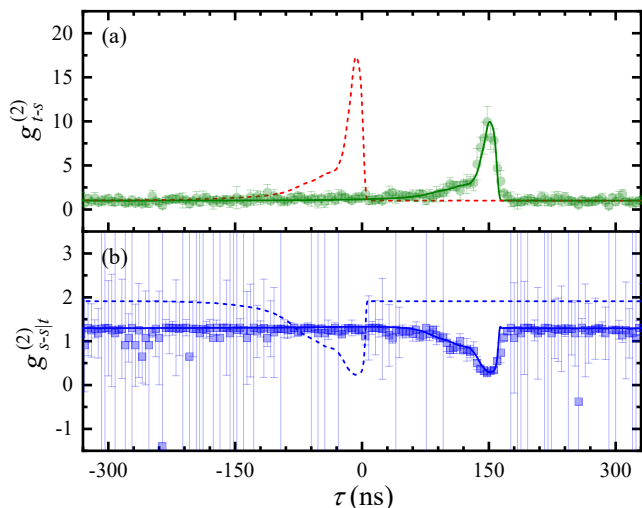


FIG. 3. Verification of quantum preservation after frequency conversion. (a) Normalized cross-correlation $g_{t-s}^{(2)}(\tau)$ between the trigger and converted signal photons, showing preserved temporal correlations after conversion. (b) Conditional autocorrelation $g_{s-s|t}^{(2)}(\tau)$ of the heralded telecom photon, confirming preservation of single-photon purity. Circles and squares denote experimental data, solid curves show theoretical predictions, and dashed curves indicate the pre-conversion results in Fig. 2. The parameters are $OD = 110$, $\Omega_c = 20\Gamma$, $\Omega_d = 12\Gamma$, $\Delta_p = -4\Gamma$, $\Delta_c = 8\Gamma$, and $\Delta_d = -5\Gamma$.

for optical leakage and detector dark counts, the peak cross-correlation reaches 18, confirming strong nonclassical correlations.

Under these conditions, the calculated generation rates of the probe and trigger photons are $R_p = 8.9 \times 10^5 \text{ s}^{-1}$ and $R_t = 1.4 \times 10^6 \text{ s}^{-1}$. The biphoton pair generation rate is $7.3 \times 10^5 \text{ s}^{-1}$, corresponding to pairing ratios of 0.82 for the probe field and 0.52 for the trigger field. The asymmetry originates from the different Clebsch–Gordan coefficients of the probe and trigger transitions, which lead to unequal photon generation rates even though correlated photon pairs are produced at the same rate. This mechanism differs from the pairing-ratio asymmetry discussed in Ref. [1], where the imbalance arises from propagation loss associated with ground-state decoherence and phase mismatch.

To further verify the single-photon character of the heralded probe photons, we evaluate the conditional autocorrelation function $g_{p-p|t}^{(2)}(\tau)$, as shown in Fig. 2(b). The minimum value reaches 0.22, confirming the nonclassical character of the heralded probe photons. The fluctuations outside the correlation window originate from low accidental coincidence counts and have negligible impact on the measurements. Since the useful quantum correlations are confined within the biphoton coherence time, the heralded photons remain suitable for interference and frequency conversion experiments.

Telecom frequency conversion. The 795 nm probe photons are converted to the 1367 nm telecom band through

diamond-type four-wave mixing (FWM) in a cold atomic ensemble. The temporal correlation between the trigger photons and the converted signal photons is characterized by the cross-correlation function $g_{t-s}^{(2)}(\tau)$, as shown in Fig. 3(a). At an OD of 110, the coupling and driving fields are $\Omega_c = 20\Gamma$ and $\Omega_d = 12\Gamma$, with detunings $\Delta_p = -4\Gamma$, $\Delta_c = 8\Gamma$, and $\Delta_d = -5\Gamma$ [29]. A peak cross-correlation of about 10 is observed, confirming that strong quantum correlations are preserved after conversion. Compared with the pre-conversion value of about 18, the reduction is mainly attributed to the higher dark-count rate of the InGaAs detector. Using the measured channel purities $P_t = 0.89$ and $P_s = 0.54$, Eq. (3) predicts a peak value of 9, which is in reasonable agreement with the measured value. The conditional autocorrelation of the converted telecom photons is shown in Fig. 3(b), with a minimum value of 0.27 that remains well below the classical limit.

To examine waveform preservation, we compare the biphoton wavepackets before and after conversion. The full width at half maximum remains about 20 ns, corresponding to a Fourier-limited spectral bandwidth of approximately 17.4 MHz, consistent with the pre-conversion result. This observation confirms that the temporal mode structure is well preserved during the conversion process. A delay of about 155 ns is observed, in agreement with the combined propagation delay from the fiber path, free-space propagation, and the group delay of the FWM process. Such a delay is consistent with the timing sequence of heralding and conversion.

Initially, the conversion efficiency is about 55%, lower than the 80% efficiency obtained using weak coherent inputs. This reduction originates from incomplete spectral overlap between the probe photons and the finite acceptance bandwidth of the conversion process. The acceptance window is approximately 40 MHz [29]. Although broader than the probe bandwidth, the conversion efficiency decreases near the spectral edges. In contrast, the spectral response of the atomic converter is nearly flat in the central high-efficiency region. Consequently, the dominant spectral components are converted efficiently, while the spectral edges mainly reduce the total photon number. The temporal waveform therefore remains well preserved despite the reduced overall efficiency.

To further improve the conversion efficiency, the SFWM bandwidth is reduced to better match the acceptance window of the converter. By tuning the source parameters to an OD of 17 with pump Rabi frequencies $\Omega_1 = 1.8\Gamma$ and $\Omega_2 = 2\Gamma$, the spectral bandwidth of the heralded probe photons is narrowed to about 2.5 MHz. At the same time, the photon generation rate remains on the order of 10^7 s^{-1} . In this regime, the probe spectrum lies well within the high-efficiency region of the conversion response, allowing both high conversion efficiency and reliable preservation of the temporal waveform.

Further optimization of the conversion system is achieved by increasing the OD to 120 and raising the coupling field to 23Γ . Figure 4 shows the conversion ef-

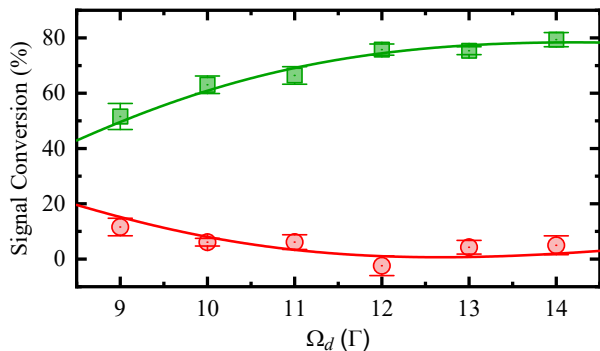


FIG. 4. High-efficiency telecom conversion enabled by spectral matching. Signal conversion efficiency and probe transmission as functions of the driving field strength. Circles denote probe transmission and squares represent signal conversion efficiency. Solid curves are theoretical predictions. The optimized source parameters are $OD = 17$, $\Omega_1 = 1.8\Gamma$, $\Omega_2 = 2\Gamma$, and $\Delta_1 = -4\Gamma$. The conversion parameters are $OD = 120$, $\Omega_c = 23\Gamma$, $\Delta_p = -4\Gamma$, $\Delta_c = 8\Gamma$, and $\Delta_d = -5\Gamma$. The reduced photon bandwidth ensures near-complete spectral overlap with the conversion window and enables high-efficiency conversion close to the steady-state limit. These results confirm that the efficiency reduction in the broadband regime mainly originates from spectral mismatch.

efficiency as a function of Ω_d . The maximum efficiency reaches 79.4(2.6)% at $\Omega_d = 14\Gamma$. These results indicate that spectral matching together with optimized conversion parameters [30] enables efficient telecom conversion of heralded single photons.

Preserving the temporal waveform is important for quantum networking. The maintained wavepacket supports high indistinguishability and efficient temporal-mode matching for Hong–Ou–Mandel interference. The narrow bandwidth also provides a long coherence length,

relaxing path-length stability requirements in fiber systems. Together with the achieved efficiency and spectral controllability, this platform offers a promising interface for Bell-state measurements and repeater-based quantum communication in telecom networks.

Conclusion. We demonstrate telecom frequency conversion of atomic biphotons while preserving their temporal waveforms and nonclassical correlations. The maintained time-resolved wavepackets show that the conversion process preserves the dynamical properties of heralded single photons beyond conventional statistical benchmarks. The experimental observations are consistent with a microscopic model that clarifies how spectral acceptance and system parameters determine the conversion performance. The demonstrated interface achieves telecom conversion efficiencies approaching 80% while maintaining the temporal waveform and quantum correlations of the biphotons.

Our results show that combining spectral engineering of the biphoton source with system-level optimization of the atomic converter provides a controllable platform for interfacing atomic quantum systems with telecom fiber networks. The simultaneous realization of spectral matching, waveform preservation, and high conversion efficiency is directly relevant for quantum repeaters, long-distance entanglement distribution, and photonic quantum networking. These results highlight temporal-mode engineering as an important design principle for future hybrid quantum systems.

Acknowledgements. We thank Y.-T. Ma, M.-Y. Lin, and X.-Q. Zhong for contributions to the initial experimental setup. This work was supported by the National Science and Technology Council of Taiwan under Grants No. 114-2112-M-006-007 and No. 114-2119-M-007-012. Support from the Center for Quantum Science and Technology under the Higher Education Sprout Project of the Ministry of Education in Taiwan is also acknowledged.

-
- [1] L.-M. Duan, M. D. Lukin, J. I. Cirac, and P. Zoller, Long-distance quantum communication with atomic ensembles and linear optics, *Nature* **414**, 413 (2001).
- [2] H.-S. Zhong, H. Wang, Y.-H. Deng, M.-C. Chen, L.-C. Peng, Y.-H. Luo, J. Qin, D. Wu, X. Ding, Y. Hu, P. Hu, X.-Y. Yang, W.-J. Zhang, H. Li, Y. Li, X. Jiang, L. Gan, G. Yang, L. You, Z. Wang, L. Li, N.-L. Liu, C.-Y. Lu, and J.-W. Pan, Quantum computational advantage using photons, *Science* **370**, 1460 (2020).
- [3] X.-M. Hu, C.-X. Huang, Y.-B. Sheng, L. Zhou, B.-H. Liu, Y. Guo, C. Zhang, W.-B. Xing, Y.-F. Huang, C.-F. Li, and G.-C. Guo, Long-distance entanglement purification for quantum communication, *Phys. Rev. Lett.* **126**, 010503 (2021).
- [4] Y. Liu, W.-J. Zhang, C. Jiang, J.-P. Chen, C. Zhang, W.-X. Pan, D. Ma, H. Dong, J.-M. Xiong, C.-J. Zhang, H. Li, R.-C. Wang, J. Wu, T.-Y. Chen, L. You, X.-B. Wang, Q. Zhang, and J.-W. Pan, Experimental twin-field quantum key distribution over 1000 km fiber distance, *Phys. Rev. Lett.* **130**, 210801 (2023).
- [5] D. Main, P. Drmota, D. P. Nadlinger, E. M. Ainley, A. Agrawal, B. C. Nichol, R. Srinivas, G. Araneda, and D. M. Lucas, Distributed quantum computing across an optical network link, *Nature* **638**, 383 (2025).
- [6] M. Pittaluga, Y. S. Lo, A. Brzosko, R. I. Woodward, D. Scalcon, M. S. Winnel, T. Roger, J. F. Dynes, K. A. Owen, S. Juárez, P. Rydlichowski, D. Vicinanza, G. Roberts, and A. J. Shields, Long-distance coherent quantum communications in deployed telecom networks, *Nature* **640**, 911 (2025).
- [7] V. Balić, D. A. Braje, P. Kolchin, G. Y. Yin, and S. E. Harris, Generation of paired photons with controllable waveforms, *Phys. Rev. Lett.* **94**, 183601 (2005).
- [8] L. Zhao, X. Guo, C. Liu, Y. Sun, M. M. T. Loy, and S. Du, Photon pairs with coherence time exceeding 1 μ s, *Optica* **1**, 84 (2014).
- [9] C.-Y. Hsu, Y.-S. Wang, J.-M. Chen, F.-C. Huang, Y.-T. Ke, E. K. Huang, W. Hung, K.-L. Chao, S.-S. Hsiao,

- Y.-H. Chen, C.-S. Chuu, Y.-C. Chen, Y.-F. Chen, and I. A. Yu, Generation of sub-MHz and spectrally-bright biphotons from hot atomic vapors with a phase mismatch-free scheme, *Opt. Express* **29**, 4632 (2021).
- [10] J.-S. Shiu, Z.-Y. Liu, C.-Y. Cheng, Y.-C. Huang, I. A. Yu, Y.-C. Chen, C.-S. Chuu, C.-M. Li, S.-Y. Wang, and Y.-F. Chen, Observation of highly correlated ultrabright biphotons through increased atomic ensemble density in spontaneous four-wave mixing, *Phys. Rev. Res.* **6**, L032001 (2024).
- [11] J.-K. Lin, T.-H. Chien, C.-T. Wu, R. Chinnarasu, S. Du, I. A. Yu, and C.-S. Chuu, Observation of subnaturallinewidth biphotons in a two-level atomic ensemble, *Phys. Rev. Lett.* **134**, 043602 (2025).
- [12] Y.-S. Wang, K.-B. Li, C.-F. Chang, T.-W. Lin, J.-Q. Li, S.-S. Hsiao, J.-M. Chen, Y.-H. Lai, Y.-C. Chen, Y.-F. Chen, C.-S. Chuu, and I. A. Yu, Temporally ultralong biphotons with a linewidth of 50 kHz, *APL Photonics* **7**, 126102 (2022).
- [13] K. S. Choi, H. Deng, J. Laurat, and H. J. Kimble, Mapping photonic entanglement into and out of a quantum memory, *Nature* **452**, 67 (2008).
- [14] D. S. Ding, Z. Y. Zhou, B. S. Shi, and G. C. Guo, Single-photon-level quantum image memory based on cold atomic ensembles, *Nat. Commun.* **4**, 2527 (2013).
- [15] Y.-W. Cho, G. T. Campbell, J. L. Everett, J. Bernu, D. B. Higginbottom, M. T. Cao, J. Geng, N. P. Robins, P. K. Lam, and B. C. Buchler, Highly efficient optical quantum memory with long coherence time in cold atoms, *Optica* **3**, 100 (2016).
- [16] T. Chanelière, D. N. Matsukevich, S. D. Jenkins, T. A. B. Kennedy, M. S. Chapman, and A. Kuzmich, Quantum telecommunication based on atomic cascade transitions, *Phys. Rev. Lett.* **96**, 093604 (2006).
- [17] R. T. Willis, F. E. Becerra, L. A. Orozco, and S. L. Rolston, Photon statistics and polarization correlations at telecommunications wavelengths from a warm atomic ensemble, *Opt. Express* **19**, 14632 (2011).
- [18] W. Zhang, D.-S. Ding, S. Shi, Y. Li, Z.-Y. Zhou, B.-S. Shi, and G.-C. Guo, Storing a single photon as a spin wave entangled with a flying photon in the telecommunication bandwidth, *Phys. Rev. A* **93**, 022316 (2016).
- [19] P.-Y. Tu, C.-Y. Hsu, W.-K. Huang, T.-Y. Lin, C.-S. Chuu, and I. A. Yu, Temporally long C-band heralded single photons generated from hot atoms, *APL Photon.* **10**, 106104 (2025).
- [20] Z.-Y. Liu, J.-S. Shiu, W.-L. Chen, and Y.-F. Chen, Microscopic origin of superradiant biphoton emission in atomic ensembles, arXiv:2602.11438 (2026).
- [21] K. Niizeki, K. Ikeda, M. Zheng, X. Xie, K. Okamura, N. Takei, N. Namekata, S. Inoue, H. Kosaka, and T. Horikiri, Ultrabright narrow-band telecom two-photon source for long-distance quantum communication, *Appl. Phys. Express* **11**, 042801 (2018).
- [22] M.-Y. Gao, Y.-H. Li, Y. Li, Z.-Y. Zhou, Z. Zhou, G.-C. Guo, and B.-S. Shi, Narrowband telecom-band polarization-entangled photon source by superposed monolithic cavities, *Phys. Rev. A* **109**, 033720 (2024).
- [23] R. T. Willis, F. E. Becerra, L. A. Orozco, and S. L. Rolston, Four-wave mixing in the diamond configuration in an atomic vapor, *Phys. Rev. A* **79**, 033814 (2009).
- [24] H. Jeong, H. Kim, J. Bae, J. Park, and H. S. Moon, Doppler-broadened four-wave mixing under double-resonance optical pumping in the $5S_{1/2}-5P_{3/2}-4D_{5/2}$ transition of warm ^{87}Rb atoms, *Opt. Express* **29**, 42384 (2021).
- [25] W.-H. Zhang, Y.-H. Ye, L. Zeng, M.-X. Dong, E.-Z. Li, J.-Y. Peng, Y. Li, D.-S. Ding, and B.-S. Shi, Telecom-wavelength conversion in a high optical depth cold atomic system, *Opt. Express* **31**, 8042 (2023).
- [26] J. A. Rowland, C. Perrella, R. F. Offer, A. N. Luiten, B. M. Sparkes, and T. J. Weinhold, Characterization of near-infrared to telecom frequency conversion in a rubidium-filled hollow-core photonic-crystal fiber, *Opt. Express* **33**, 18076 (2025).
- [27] A. G. Radnaev, Y. O. Dudin, R. Zhao, H. H. Jen, S. D. Jenkins, A. Kuzmich, and T. A. B. Kennedy, A quantum memory with telecom-wavelength conversion, *Nature Phys.* **6**, 894 (2010).
- [28] Y. O. Dudin, A. G. Radnaev, R. Zhao, J. Z. Blumoff, T. A. B. Kennedy, and A. Kuzmich, Entanglement of light-shift compensated atomic spin waves with telecom light, *Phys. Rev. Lett.* **105**, 260502 (2010).
- [29] L.-C. Chen, M.-Y. Lin, J.-S. Shiu, X.-Q. Zhong, P.-H. Tseng, and Y.-F. Chen, High-efficiency telecom frequency conversion via a diamond-type atomic ensemble, *Phys. Rev. A* **112**, 013709 (2025).
- [30] P.-H. Tseng, L.-C. Chen, J.-S. Shiu, and Y.-F. Chen, Quantum interface for telecom frequency conversion based on diamond-type atomic ensembles, *Phys. Rev. A* **109**, 043716 (2024).
- [31] C. K. Hong, Z. Y. Ou, and L. Mandel, Measurement of subpicosecond time intervals between two photons by interference, *Phys. Rev. Lett.* **59**, 2044 (1987).
- [32] H. Ollivier, S. E. Thomas, S. C. Wein, I. Maillette de Buy Wenniger, N. Coste, J. C. Loredó, N. Somaschi, A. Harouri, A. Lemaitre, I. Sagnes, L. Lanco, C. Simon, C. Anton, O. Krebs, and P. Senellart, Hong-Ou-Mandel interference with imperfect single photon sources, *Phys. Rev. Lett.* **126**, 063602 (2021).
- [33] E. Arenskötter, S. Kucera, O. Elshehy, M. Bergerhoff, M. Kreis, L. Brunel, and J. Eschner, Full Bell-basis measurement of an atom-photon 2-qubit state and its application for quantum networks, *Phys. Rev. Res.* **6**, 023061 (2024).
- [34] N. Hauser, M. J. Bayerbach, S. E. D'Aurelio, R. Weber, M. Santandrea, S. P. Kumar, I. Dhand, and S. Barz, Boosted Bell-state measurements for photonic quantum computation, *npj Quantum Inf.* **11**, 41 (2025).
- [35] J.-S. Shiu, C.-W. Lin, Y.-C. Huang, M.-J. Lin, I. C. Huang, T.-H. Wu, P.-C. Kuan, and Y.-F. Chen, Frequency-tunable biphoton generation via spontaneous four-wave mixing, *Phys. Rev. A* **110**, 063723 (2024).
- [36] J.-S. Shiu, C.-W. Lin, and Y.-F. Chen, Asymmetric biphoton generation under ground-state decoherence and phase mismatch in a cold atomic ensemble, *Adv. Quantum Technol.* **8**, e2500052 (2025).

Supplemental Material for Quantum-preserving telecom conversion of atomic biphotons

Ling-Chun Chen, Chang-Wei Lin, Jiun-Shiuan Shiu, Wei-Lin Chen, Yi-Che Wang, and Yong-Fan Chen*

¹*Department of Physics, National Cheng Kung University, Tainan 70101, Taiwan*

²*Center for Quantum Frontiers of Research & Technology, Tainan 70101, Taiwan*

This Supplemental Material presents the derivation of the corrected conditional autocorrelation function $g_{p-p|t}^{(2)}(\tau)$ under realistic experimental conditions. To account for background counts and detector dark noise, the detected fields are modeled as a linear superposition of statistically independent signal and noise operators. By introducing channel purities (P_t, P_p) that quantify the fraction of genuine biphoton events, the coincidence expectation values are systematically evaluated. The resulting analytical expression relates the measured correlation function to the intrinsic quantum statistics and correctly recovers the noise-free limit.

To quantify the single-photon purity of the heralded probe field, we evaluate the conditional autocorrelation function defined as [S1]

$$g_{p-p|t}^{(2)}(\tau) = \frac{\langle \hat{a}_t^\dagger(t) \hat{a}_t(t) \rangle \langle \hat{a}_t^\dagger(t) \hat{a}_{p1}^\dagger(t+\tau) \hat{a}_{p2}^\dagger(t+\tau) \hat{a}_{p2}(t+\tau) \hat{a}_{p1}(t+\tau) \hat{a}_t(t) \rangle}{\langle \hat{a}_t^\dagger(t) \hat{a}_{p1}^\dagger(t+\tau) \hat{a}_{p1}(t+\tau) \hat{a}_t(t) \rangle \langle \hat{a}_t^\dagger(t) \hat{a}_{p2}^\dagger(t+\tau) \hat{a}_{p2}(t+\tau) \hat{a}_t(t) \rangle}. \quad (\text{S1})$$

Here $p1$ and $p2$ denote the two probe detection channels in the Hanbury Brown–Twiss (HBT) configuration. The delay τ represents the relative detection time between the probe and trigger photons. In the ideal limit where only correlated photon pairs are detected, the conditional autocorrelation reduces to $g_{p-p|t}^{(2)}(\tau) = [4g_{t-p}^{(2)}(\tau) - 2][g_{t-p}^{(2)}(\tau)]^{-2}$.

The second-order cross-correlation function is $g_{t-p}^{(2)}(\tau) = \langle \hat{a}_t^\dagger \hat{a}_p^\dagger \hat{a}_p \hat{a}_t \rangle \langle \hat{a}_t^\dagger \hat{a}_t \rangle^{-1} \langle \hat{a}_p^\dagger \hat{a}_p \rangle^{-1}$.

To account for experimental imperfections in the correlation measurements, we decompose the annihilation operator of each detection channel $l \in \{t, p1, p2\}$ into signal and noise contributions, $\hat{a}_l = \hat{a}_{l,b} + \hat{a}_{l,e}$. Here the subscript b denotes the genuine biphoton signal, while e represents environmental noise such as background light and detector dark counts. The biphoton signal and environmental noise are assumed to be statistically independent, and noise contributions in different spatial channels are also independent. Consequently, the cross-term expectation values vanish, $\langle \hat{a}_{l,b}^\dagger \hat{a}_{l,e} \rangle = \langle \hat{a}_{l,e}^\dagger \hat{a}_{l,b} \rangle = \langle \hat{a}_{l,b} \hat{a}_{l,e} \rangle = \langle \hat{a}_{l,e} \hat{a}_{l,b} \rangle = 0$, and $\langle \hat{a}_{m,e}^\dagger \hat{a}_{n,e} \rangle = 0$ ($m \neq n$).

With the statistical independence between the biphoton signal and environmental noise established, we now evaluate the expectation values appearing in the conditional autocorrelation function of Eq. (S1). Substituting the decomposed operators for each detection channel and removing the vanishing cross terms yields the following expressions:

■ Trigger-channel intensity $\langle \hat{a}_t^\dagger \hat{a}_t \rangle$

$$\langle \hat{a}_t^\dagger \hat{a}_t \rangle = \langle (\hat{a}_{t,b}^\dagger + \hat{a}_{t,e}^\dagger)(\hat{a}_{t,b} + \hat{a}_{t,e}) \rangle = \langle \hat{a}_{t,b}^\dagger \hat{a}_{t,b} \rangle + \langle \hat{a}_{t,e}^\dagger \hat{a}_{t,e} \rangle. \quad (\text{S2})$$

■ Two-fold coincidence (probe channel 1) $\langle \hat{a}_t^\dagger \hat{a}_{p1}^\dagger \hat{a}_{p1} \hat{a}_t \rangle$

$$\begin{aligned} \langle \hat{a}_t^\dagger \hat{a}_{p1}^\dagger \hat{a}_{p1} \hat{a}_t \rangle &= \langle (\hat{a}_{t,b}^\dagger + \hat{a}_{t,e}^\dagger)(\hat{a}_{p1,b}^\dagger + \hat{a}_{p1,e}^\dagger)(\hat{a}_{p1,b} + \hat{a}_{p1,e})(\hat{a}_{t,b} + \hat{a}_{t,e}) \rangle \\ &= \langle (\hat{a}_{t,b}^\dagger \hat{a}_{p1,b}^\dagger + \hat{a}_{t,b}^\dagger \hat{a}_{p1,e}^\dagger + \hat{a}_{t,e}^\dagger \hat{a}_{p1,b}^\dagger + \hat{a}_{t,e}^\dagger \hat{a}_{p1,e}^\dagger)(\hat{a}_{p1,b} \hat{a}_{t,b} + \hat{a}_{p1,b} \hat{a}_{t,e} + \hat{a}_{p1,e} \hat{a}_{t,b} + \hat{a}_{p1,e} \hat{a}_{t,e}) \rangle \\ &= \langle \hat{a}_{t,b}^\dagger \hat{a}_{p1,b}^\dagger \hat{a}_{p1,b} \hat{a}_{t,b} \rangle + \langle \hat{a}_{t,b}^\dagger \hat{a}_{p1,e}^\dagger \hat{a}_{p1,e} \hat{a}_{t,b} \rangle + \langle \hat{a}_{t,e}^\dagger \hat{a}_{p1,b}^\dagger \hat{a}_{p1,b} \hat{a}_{t,e} \rangle + \langle \hat{a}_{t,e}^\dagger \hat{a}_{p1,e}^\dagger \hat{a}_{p1,e} \hat{a}_{t,e} \rangle \\ &= \langle \hat{a}_{t,b}^\dagger \hat{a}_{p1,b}^\dagger \hat{a}_{p1,b} \hat{a}_{t,b} \rangle + \langle \hat{a}_{t,b}^\dagger \hat{a}_{t,b} \rangle \langle \hat{a}_{p1,e}^\dagger \hat{a}_{p1,e} \rangle + \langle \hat{a}_{t,e}^\dagger \hat{a}_{t,e} \rangle \langle \hat{a}_{p1,b}^\dagger \hat{a}_{p1,b} \rangle + \langle \hat{a}_{t,e}^\dagger \hat{a}_{t,e} \rangle \langle \hat{a}_{p1,e}^\dagger \hat{a}_{p1,e} \rangle \\ &= \langle \hat{a}_{t,b}^\dagger \hat{a}_{t,b} \rangle \langle \hat{a}_{p1,b}^\dagger \hat{a}_{p1,b} \rangle g_{t-p}^{(2)} + \langle \hat{a}_{t,b}^\dagger \hat{a}_{t,b} \rangle \langle \hat{a}_{p1,e}^\dagger \hat{a}_{p1,e} \rangle + \langle \hat{a}_{t,e}^\dagger \hat{a}_{t,e} \rangle \langle \hat{a}_{p1,b}^\dagger \hat{a}_{p1,b} \rangle + \langle \hat{a}_{t,e}^\dagger \hat{a}_{t,e} \rangle \langle \hat{a}_{p1,e}^\dagger \hat{a}_{p1,e} \rangle \\ &= (\langle \hat{a}_{t,b}^\dagger \hat{a}_{t,b} \rangle + \langle \hat{a}_{t,e}^\dagger \hat{a}_{t,e} \rangle) (\langle \hat{a}_{p1,b}^\dagger \hat{a}_{p1,b} \rangle + \langle \hat{a}_{p1,e}^\dagger \hat{a}_{p1,e} \rangle) + \langle \hat{a}_{t,b}^\dagger \hat{a}_{t,b} \rangle \langle \hat{a}_{p1,b}^\dagger \hat{a}_{p1,b} \rangle [g_{t-p}^{(2)} - 1]. \quad (\text{S3}) \end{aligned}$$

To simplify the notation, we introduce the mean photon numbers $n_{l,x} = \langle \hat{a}_{l,x}^\dagger \hat{a}_{l,x} \rangle$, where $l \in \{t, p1, p2\}$ denotes the detection channel and $x \in \{b, e\}$ distinguishes the biphoton signal from environmental noise. We also define the channel purity $P_l = n_{l,b}/(n_{l,b} + n_{l,e})$, which quantifies the fraction of genuine biphoton events in the detected counts. With these definitions, the two-fold coincidence rate in Eq. (S3) can be written as $\langle \hat{a}_t^\dagger \hat{a}_{p1}^\dagger \hat{a}_{p1} \hat{a}_t \rangle = (n_{t,b} + n_{t,e})(n_{p1,b} + n_{p1,e})\{P_t P_{p1}[g_{t-p}^{(2)} - 1] + 1\}$.

■ **Two-fold coincidence (probe channel 2)** $\langle \hat{a}_t^\dagger \hat{a}_{p2}^\dagger \hat{a}_{p2} \hat{a}_t \rangle$

$$\begin{aligned} \langle \hat{a}_t^\dagger \hat{a}_{p2}^\dagger \hat{a}_{p2} \hat{a}_t \rangle &= \langle (\hat{a}_{t,b}^\dagger + \hat{a}_{t,e}^\dagger)(\hat{a}_{p2,b}^\dagger + \hat{a}_{p2,e}^\dagger)(\hat{a}_{p2,b} + \hat{a}_{p2,e})(\hat{a}_{t,b} + \hat{a}_{t,e}) \rangle \\ &= (n_{t,b} + n_{t,e})(n_{p2,b} + n_{p2,e})\{P_t P_{p2}[g_{t-p}^{(2)} - 1] + 1\}. \end{aligned} \quad (\text{S4})$$

In a standard HBT configuration, the 50/50 beam splitter ensures that the two probe detection paths have identical statistical properties and noise levels. The corresponding channel purities are therefore equal. For notational simplicity we denote $n_{p1,b} = n_{p2,b} \equiv n_{p,b}$, $n_{p1,e} = n_{p2,e} \equiv n_{p,e}$, and $P_{p1} = P_{p2} \equiv P_p$.

■ **Three-fold coincidence** $\langle \hat{a}_t^\dagger \hat{a}_{p1}^\dagger \hat{a}_{p2}^\dagger \hat{a}_{p2} \hat{a}_{p1} \hat{a}_t \rangle$

$$\begin{aligned} \langle \hat{a}_t^\dagger \hat{a}_{p1}^\dagger \hat{a}_{p2}^\dagger \hat{a}_{p2} \hat{a}_{p1} \hat{a}_t \rangle &= \langle (\hat{a}_{t,b}^\dagger + \hat{a}_{t,e}^\dagger)(\hat{a}_{p1,b}^\dagger + \hat{a}_{p1,e}^\dagger)(\hat{a}_{p2,b}^\dagger + \hat{a}_{p2,e}^\dagger)(\hat{a}_{p2,b} + \hat{a}_{p2,e})(\hat{a}_{p1,b} + \hat{a}_{p1,e})(\hat{a}_{t,b} + \hat{a}_{t,e}) \rangle \\ &= \langle \hat{a}_{t,b}^\dagger \hat{a}_{p1,b}^\dagger \hat{a}_{p2,b}^\dagger \hat{a}_{p2,b} \hat{a}_{p1,b} \hat{a}_{t,b} \rangle \\ &\quad + \langle \hat{a}_{t,b}^\dagger \hat{a}_{p1,b}^\dagger \hat{a}_{p2,b}^\dagger \hat{a}_{p2,b} \hat{a}_{t,b} \rangle \langle \hat{a}_{p1,e}^\dagger \hat{a}_{p1,e} \rangle + \langle \hat{a}_{p1,b}^\dagger \hat{a}_{p2,b}^\dagger \hat{a}_{p2,b} \hat{a}_{p1,b} \rangle \langle \hat{a}_{t,e}^\dagger \hat{a}_{t,e} \rangle \\ &\quad + \langle \hat{a}_{t,b}^\dagger \hat{a}_{t,b} \rangle \langle \hat{a}_{p1,e}^\dagger \hat{a}_{p1,e} \rangle \langle \hat{a}_{p2,e}^\dagger \hat{a}_{p2,e} \rangle + \langle \hat{a}_{p1,b}^\dagger \hat{a}_{p1,b} \rangle \langle \hat{a}_{t,e}^\dagger \hat{a}_{t,e} \rangle \langle \hat{a}_{p2,e}^\dagger \hat{a}_{p2,e} \rangle + \langle \hat{a}_{p2,b}^\dagger \hat{a}_{p2,b} \rangle \langle \hat{a}_{t,e}^\dagger \hat{a}_{t,e} \rangle \langle \hat{a}_{p1,e}^\dagger \hat{a}_{p1,e} \rangle \\ &\quad + \langle \hat{a}_{t,e}^\dagger \hat{a}_{t,e} \rangle \langle \hat{a}_{p1,e}^\dagger \hat{a}_{p1,e} \rangle \langle \hat{a}_{p2,e}^\dagger \hat{a}_{p2,e} \rangle \\ &= [4g_{t-p}^{(2)} - 2][g_{t-p}^{(2)}]^{-2} \langle \hat{a}_{t,b}^\dagger \hat{a}_{p1,b}^\dagger \hat{a}_{p1,b} \hat{a}_{t,b} \rangle \langle \hat{a}_{t,b}^\dagger \hat{a}_{p2,b}^\dagger \hat{a}_{p2,b} \hat{a}_{t,b} \rangle \langle \hat{a}_{t,b} \hat{a}_{t,b} \rangle^{-1} \\ &\quad + [2n_{t,b} n_{p,b} n_{p,e} g_{t-p}^{(2)} + 2n_{p,b}^2 n_{t,e}] + (n_{t,b} n_{p,e}^2 + 2n_{p,b} n_{t,e} n_{p,e}) + n_{t,e} n_{p,e}^2 \\ &= 4n_{t,b} n_{p,b}^2 [g_{t-p}^{(2)} - 1] + 2n_{t,b} n_{p,b}^2 \\ &\quad + 2n_{t,b} n_{p,b} n_{p,e} [g_{t-p}^{(2)} - 1] + 2n_{t,b} n_{p,b} n_{p,e} + 2n_{p,b}^2 n_{t,e} + n_{t,b} n_{p,e}^2 + 2n_{p,b} n_{t,e} n_{p,e} + n_{t,e} n_{p,e}^2 \\ &= 2n_{t,b} n_{p,b} (2n_{p,b} + n_{p,e}) [g_{t-p}^{(2)} - 1] + (n_{t,b} + n_{t,e}) [n_{p,b}^2 + (n_{p,b} + n_{p,e})^2]. \end{aligned} \quad (\text{S5})$$

Substituting Eqs. (S2)–(S5) into Eq. (S1) gives the zero-delay conditional autocorrelation function

$$\begin{aligned} g_{p-p|t}^{(2)} &= \frac{(n_{t,b} + n_{t,e})\{2n_{t,b} n_{p,b} (2n_{p,b} + n_{p,e}) [g_{t-p}^{(2)} - 1] + (n_{t,b} + n_{t,e}) [n_{p,b}^2 + (n_{p,b} + n_{p,e})^2]\}}{(n_{t,b} + n_{t,e})^2 (n_{p,b} + n_{p,e})^2 \{P_t P_p [g_{t-p}^{(2)} - 1] + 1\}^2} \\ &= \frac{1 + P_p^2 + 2P_t P_p (1 + P_p) [g_{t-p}^{(2)} - 1]}{\{P_t P_p [g_{t-p}^{(2)} - 1] + 1\}^2}, \end{aligned} \quad (\text{S6})$$

which is consistent with Eq. (4) of the main text.

[S1] J.-S. Shiu, C.-W. Lin, and Y.-F. Chen, Asymmetric biphoton generation under ground-state decoherence and phase mismatch in a cold atomic ensemble, *Adv. Quantum Technol.* **8**, e2500052 (2025).